



Superresolution MRI with a Structured-Illumination Approach

Rui Tian (田锐)^{*}, Franciszek Hennel, Samuel Bianchi, and Klass P. Pruessmann
Institute for Biomedical Engineering, ETH Zurich and University of Zurich, Zurich, Switzerland

 (Received 16 April 2022; revised 6 December 2022; accepted 2 February 2023; published 23 March 2023; corrected 19 April 2023)

Unlike optical imaging methods, where the Fourier representation of the object is created by wave diffraction, magnetic resonance imaging (MRI) scans the Fourier domain by spatially modulating the nuclear magnetization with magnetic field gradients. Therefore, the resolution of MRI is limited by signal strength rather than the wavelength of the diffracted wave. However, in several important applications, such as the imaging of water diffusion or blood oxygenation in the human brain, MRI must collect all the Fourier data during a single evolution of the signal to avoid artifacts caused by random fluctuations of its phase. The Fourier domain coverage of the “single-shot” MRI strategy is limited by the lifetime of the signal and results in a resolution limit analogous to the diffraction limit in optical microscopy. Consequently, recently developed optical superresolution methods may appear helpful. This work employs the recently developed method of phaseless encoding, which implements the idea of linear structured illumination microscopy (SIM) to enable multishot data acquisition and triple the MRI resolution regardless of the presence of spin phase fluctuations, and develops it further to enhance the resolution in two dimensions and to push its gain above a factor of 3 using “illumination patterns” with multiple harmonics, a concept borrowed from saturated SIM (SSIM) methodology. Results obtained with enhanced phaseless encoding on a 3-Tesla clinical scanner in phantoms and human brain are presented. This method will be beneficial when conventional multishot MRI is impeded by signal instability due to motion or other factors.

DOI: [10.1103/PhysRevApplied.19.034074](https://doi.org/10.1103/PhysRevApplied.19.034074)

I. INTRODUCTION

The kinship of magnetic resonance imaging (MRI) with Fourier optics, noticed by Lauterbur [1] and Mansfield [2] in their seminal 1973 papers, inspired several concepts during the early years of development of this technique, greatly contributing to its present status as a standard medical imaging tool. Decades later, the breathtaking progress made in the meantime by optical microscopy and the advent of superresolution (SR) methods overcoming the diffraction limit (i.e., the Abbe or the Rayleigh criterion) again provide ideas that allow MRI performance to be pushed higher in some of its important applications.

A. The diffraction limit in MRI

Mansfield has proposed to describe MRI using terms of diffraction physics [3] and this approach is used ever since. MRI scanners create transverse nuclear magnetization in an object by exciting polarized spins with a radio-frequency (rf) pulse, modulate it by letting the spins precess in the presence of a gradient field superimposed on the main field of the polarizing magnet, and measure a signal that is given by the net magnetization. This allows sampling of the object’s

representation in the Fourier domain, called k space, along a trajectory whose speed is defined by shaped pulses of three orthogonal gradients [4–6]. The shortest modulation period, and thus the maximum k -space range, which sets the resolution limit, does not depend on the resonance frequency or electromagnetic wavelength, as is the case in optical microscopy where the Fourier domain signal is created by diffraction. In MRI, the resolution limit is solely defined by the strength of the magnetic field gradient and the lifetime of the precession signal. With gradients available on modern scanners (almost 0.1 T/m) and transverse relaxation times of ^1H nuclei in the water in tissue of tens of milliseconds, the k -space range that can be reached with a straight trajectory section corresponds to a resolution limit of a few microns, well below the detection level of MRI receiver coils, which is roughly 100–200 μm . Because multiple trajectory sections are needed to sample two-dimensional (2D) k space, high-resolution MRI uses multiple spin excitations, or “shots,” to collect data for one image. The resolution of multishot MRI is thus considered limited only by the signal-to-noise ratio (SNR), and free of inherent Fourier domain limits.

The situation is different when the MRI signal phase is affected by uncontrollable factors such as subject motion or respiration-induced fluctuations of the magnetic field [7]. This is particularly the case in two important neuroimaging applications: diffusion tensor MRI, a method allowing

^{*}rui.tian@tuebingen.mpg.de

neuronal connections to be traced [8], and blood-oxygenation-level-dependent (BOLD) MRI used to observe cortical activity [9–11]. These applications usually require the entire image information to be scanned with a single shot, and use a long 2D k -space trajectory, which takes the form of a zigzag line, as in Mansfield’s popular echo planar imaging (EPI) method [12], or a spiral [13]. The k -space range covered by such trajectories is inevitably much more restricted and, with available gradient hardware, corresponds to a resolution limit of only about 1–2 mm. These circumstances place MRI in the situation of classical optics: the signal is strong enough to push the resolution higher, but a physical obstacle analogous to the diffraction limit precludes the acquisition of higher spatial frequencies.

B. Inspiration from superresolution light microscopy

Breaking the diffraction limit by superresolution optics, an achievement awarded with the 2014 Nobel Prize in chemistry, is based on a “manipulation” of the light-emitting object at a scale that is smaller than the width of the optical filter. This manipulation involves either inducing a single-point light emission in a line-scanning [14–16] or stochastic [17,18] order, or an illumination of the object with a periodic pattern that shifts normally truncated spatial frequencies into the filter’s limited bandwidth. This approach, known as structured illumination microscopy (SIM) [19–21], provides lower resolution gain than the single-point methods owing to the limitation of the achievable modulation frequency by the light wavelength, a limitation mitigated in saturated SIM (SSIM) based on nonlinear pattern distortions to generate higher-order harmonics [22–24]. However, it is the SIM principle that appears attractive in MRI, where periodic modulations are easily implemented with gradient and rf pulse sequences and used, e.g., to evaluate cardiac motion with moving “tags” [25].

In the MRI method called phaseless encoding, a microscopic sinusoidal tagging pattern is imposed on the longitudinal magnetization of the object prior to a single-shot imaging sequence [26,27]. Just like the structured illumination pattern in linear SIM, this tagging simultaneously excites three signal bands in the k space, and allows a resolution enhancement of a factor of 3. To reconstruct a high-resolution image, several low-resolution scans with different tagging shifts are required to allow the mixed bands to be separated. The acquisition thus consists of multiple shots; however, by contrast to the standard multishot MRI methods, phaseless encoding involves only a real-valued modulation. Consequently, random phase fluctuations, the “curse” of multishot MRI, can be eliminated by simply taking the magnitude of the low-resolution images acquired with each pattern shift. These images are Fourier transformed back to k space where the three band

signals are separated by inversion of a linear problem analogous to that of SIM, and, finally, an image with up to threefold resolution enhancement can be reconstructed. To improve the matrix conditioning and thus maximize the SNR of the reconstructed image, the contributions of the three signal bands are usually made equal by employing the “magic angle” (circa 54.74°) as the tagging flip angle [28].

It should be noted that the word “phase” in this context refers to the direction of the transverse spin magnetization. The proposed encoding is “phaseless” because, unlike standard MRI methods, it affects longitudinal magnetization only. The shift of the sinusoidal tagging pattern needed for phaseless encoding can also be regarded as a “phase shift”; however, since this does not involve spin phase modulation, the term “shift” is used for pattern modulations to avoid ambiguity. We also use the term “phaseless encoding” interchangeably with “superresolution MRI” to emphasize the mentioned analogy of this approach with SR optics, and to keep the established use of the SR classification in MRI for methods based on magnitude image processing [29,30].

Phaseless encoding has been successfully implemented to produce high-resolution EPI scans with diffusion weighting [28]. However, in the experiments carried out so far, the resolution enhancement was restricted to one dimension, and limited by a factor of 3. This one-dimensional (1D) improvement was well suited to the rectangular k -space coverage characteristic of EPI. Other sampling trajectories, like the spiral scan, require a more general structured illumination scheme that could give an isotropic 2D resolution enhancement. Further, to surpass the enhancement factor of 3, the signal encoding scheme should give access to more distant k -space regions. In this paper, another few phaseless encoding schemes fulfilling these criteria are developed by adapting further concepts from optical microscopy. An early account of this work was recently presented in conference abstracts [31,32]. Another application where MRI is predominantly used with single-shot sampling due to possible phase variability is functional brain imaging [9–11]. Since the blood-oxygenation contrast used in functional MRI (fMRI) requires a long gradient-echo time [9], the magnetization phase becomes highly sensitive to magnetic field offsets caused by respiration and heartbeat [7]. The results obtained with phaseless encoding in diffusion MRI suggest that this method should also be useful to push the resolution of fMRI and other long gradient-echo applications, such as susceptibility MRI [33].

C. MRI with 2D SIM and SSIM

First, phaseless encoding is extended to increase the resolution threefold in two orthogonal dimensions, which allows further shortening of the sampling time in each

cycle, in a manner that is compatible with both rectangular and circular k -space sampling and is thus suitable for both EPI and spiral scans. For this purpose, a total of nine k -space regions (i.e., “tiles”) can be mixed in various ways. The enhancement can be achieved by a rotational 1D tagging modulation as in SIM, with an optional scaling of the tagging along the diagonal. Alternatively, the same goal can be reached by a 2D grid tagging with shifts similar to the modulation scheme in multidoughnut nanoscopy [34]. Both strategies are implemented and compared for the trade-off between the relative SNR and the minimum scan time. Additionally, owing to the overlapping of the nine k -space regions, these parts of the data can be used to estimate any residual constant phase shifts of tagging and remove these shifts during postprocessing.

Second, the fundamental concept of SSIM is translated to phaseless encoding MRI to increase the superresolution factor. SSIM generates higher spatial harmonics by increasing the illumination power so that the sample emission signal is modulated by a nonsinusoidal function, even though the illumination pattern is diffraction limited. In MRI, however, the tagging modulation frequency, which is determined by the time integral area of the tagging gradient pulse, can be made nearly arbitrarily high. Therefore, instead of building a tagging sequence that excites all required harmonics, we apply the standard sinusoidal tag a few times (twice in the current implementation) with different wavelengths to sample harmonics of different orders one by one. In the k -space perspective, this causes mixing of the central band with two neighboring sidebands in the first scan, and two bands at twice this distance in the second, both sampled by the same elongated EPI trajectory. In each scan, the three elongated bands are resolved based on three tagging shifts, as in the standard phaseless encoded reconstruction. In this way, a fivefold superresolved image can be obtained by simply combining the signal bands reconstructed from a total of six scans (with the central band, measured twice, being averaged). Higher enhancement factors can also be envisaged.

II. IMAGING METHODOLOGY AND RESULTS

Superresolution MRI scans using the proposed techniques are carried out with a water phantom with immersed silicon tubes (1.5-mm wall thickness), a spherical water-filled phantom, and a human subject in a 3-Tesla MRI scanner. In each signal encoding scheme described in the following, the two-pulse tagging sequence for spatial modulation of magnetization (SPAMM) [25] is added at the beginning of the vendor-designed pulse sequences for EPI and spiral scans to gain access to additional k -space bands at a programmable distance and angle. A superresolution image is reconstructed by adapting the standard reconstruction pipeline for 1D phaseless encoding [28] to resolve the mixed band signals in each shot, and combining

them properly in k space. Eventually, the experiments successfully achieve nearly threefold superresolution in 2D mode and fivefold in 1D. A small band overlapping is used to avoid k -space holes similar to the multishot segmented scan. To estimate the trade-off in the SNR drop, a theoretical SNR calculation for each scheme is made, assuming an equal amplitude for the excited k -space signal bands to consider the minimum noise propagation in the reconstruction for each scan. The mathematical formulation, the technical details for all encoding schemes, and the SNR analysis are provided in the Supplemental Material [35], and the details of the implemented scan protocols and reconstruction steps are available in Sec. III. Throughout the paper, the resolution of the reconstructed images is derived as the inverse of the k -space range obtained from the phaseless encoding reconstruction. This theoretical measure agrees with the analysis of the test object contours using an extended version of the method proposed in Ref. [36], as described in the Appendix.

A. Scheme A, 2D superresolution, 1D rotational tagging

1. Tagging sequence

Scheme A applies a 1D sinusoidal tagging with four rotations, and three shifts in each direction [see Fig. 1(a)], exactly resembling the modulation patterns in the linear SIM for 2D resolution improvements. The rotation of the tagging is obtained by a linear combination of two orthogonal gradients in the SPAMM [25] sequence prior to each shot of the acquisition. In this way, standard 1D phaseless encoding scans along the four directions (i.e., horizontal, vertical, and diagonal) are consecutively performed, with optional scaling of the tagging wavelength (i.e., inversely proportional to the neighboring bands’ distance) in diagonal directions. For spiral sampling with unscaled tagging [see Fig. 1(b)], k -space data covered by a circularly arranged pattern of round tiles can be eventually reconstructed to reach threefold isotropic resolution enhancement [see Fig. 1(c)]. With Cartesian sampling, the wavelength of the diagonal tagging is shortened by a factor of $\sqrt{2}$ [see Fig. 1(d)], covering a 3×3 rectangular pattern of square tiles of reconstructed k -space data [see Fig. 1(e)], which also improves resolution threefold along two orthogonal dimensions.

2. Reconstruction: Spiral

The water phantom with silicon tubes is used to test the rotational tagging with spiral sampling [see Figs. 2(a)–2(c)]. With three acquisition shots using a low-resolution spiral window [see Fig. 2(a), black solid trajectory], regions covered by three round tiles with 14.2% band overlapping are reconstructed along each rotational direction and combined (the central band being averaged 4 times) to yield an isotropic threefold increase of the

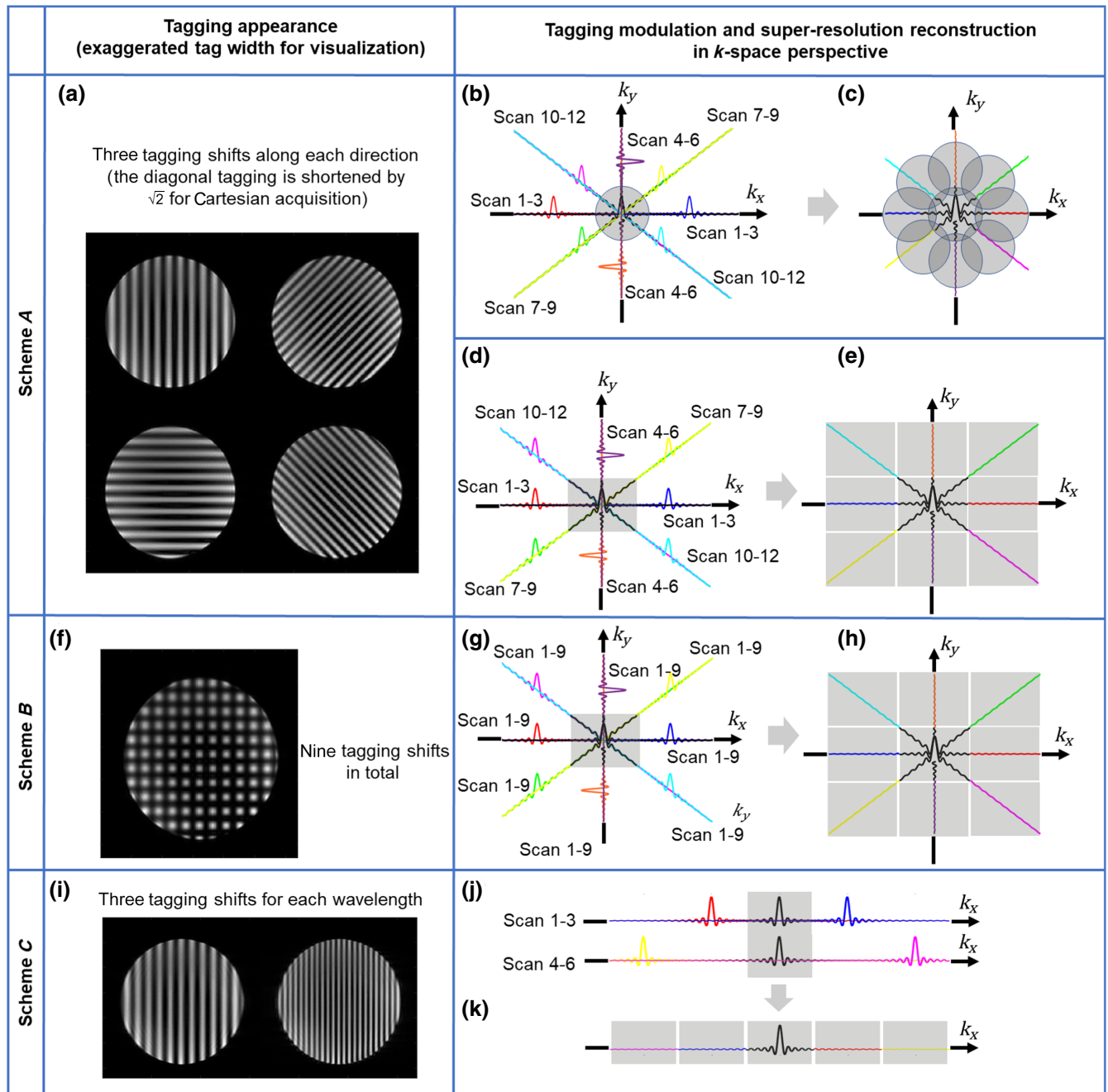


FIG. 1. Tagging modulation in the phaseless encoding schemes *A*, *B*, and *C*. (a) 1D rotated tagging with three shifts along each of the four directions, optionally with scaling of the tagging wavelength in the diagonal. (b) The k -space sampling of the mixture of the three signal bands (in distinct colors) excited along a rotated direction in a spiral trajectory. Along each direction, three scans with distinct tagging shifts are performed. (c) Reconstructed k -space data combine resolved bands from twelve scans, improving 2D coverage threefold with a rotated circular pattern. (d) The k -space sampling of the mixture of the three signal bands (in distinct colors) along a direction in a Cartesian trajectory (e.g., EPI). Along each direction, three scans with tagging shifts are performed. (e) Reconstructed k -space data improve resolution in 2D threefold with a rectangular pattern. (f) 2D grid tagging with nine tagging shifts in two orthogonal dimensions. (g) The k -space sampling of the mixture of the nine signal bands (in distinct colors) excited at a time in a Cartesian trajectory. Nine scans are performed with tagging shifts in 2D. (h) Reconstructed k -space data have a 3 times increased coverage in 2D with a rectangular pattern. (i) 1D tagging with three shifts in three scans, repeated twice. The tagging wavelength is shortened by half in the second set of three scans to excite higher-order k -space signal bands, with no need to create a saturated sinusoidal tagging as in the SSIM. (j) The k -space sampling of the three signal bands excited at a time in a Cartesian trajectory. The first three scans mix the two neighboring bands with the central band, while the second three mix the two bands twice the distance in the same sampling window. (k) The k -space reconstructed data combine resolved bands from six scans, improving resolution fivefold in 1D.

k -space coverage in the finally reconstructed data [see Fig. 2(a), side bands in red, blue, green, and gold dotted trajectories]. From a total of 12 tagged low-resolution images [$3.0 \times 3.0 \text{ mm}^2$, their sum is shown in Fig. 2(b)], a high-resolution image with resolution of $1.1 \times 1.1 \text{ mm}^2$ is reconstructed, corresponding to an almost threefold isotropic resolution improvement and resolving details that are invisible in the low-resolution scans without observable artifacts [see Fig. 2(c)].

3. Reconstruction: Cartesian

In vivo measurements are conducted to test the rotational tagging with Cartesian sampling for nonweighted images and diffusion-weighted images of the human brain with a total of 16 diffusion directions [see Figs. 2(d)–2(h)]. With three shots of low-resolution Cartesian sampling [see Fig. 2(d), black solid trajectory], k -space data covered by three square tiles are reconstructed along a tagging direction (the central band, averaged 4 times), and are combined to give a final image with nearly threefold resolution enhancement along two orthogonal dimensions [Fig. 2(d), side bands in red, blue, green, and gold dotted trajectories]. From a total of 12 low-resolution scans [$2.1 \times 2.1 \text{ mm}^2$, the sum images in Figs. 2(e) and 2(g)], a high-resolution image with resolution of $0.75 \times 0.75 \text{ mm}^2$ (approximately 10% band overlapping) is reconstructed [see Figs. 2(f) and 2(h)] with no observable artifacts. The reconstructed diffusion image [see Fig. 2(h)], which is completely free of the ghost artifacts, confirms the insensitivity of our approach to random phase fluctuations.

4. The scalable tagging wavelength in the diagonal

The scaling of the diagonal tagging in Fig. 1(d) maximizes the finally reconstructed k -space coverage with Cartesian sampling as in Fig. 1(e). However, for the phaseless encoding with spiral trajectory, simultaneous sampling of equidistant neighboring tiles in all directions turns out to be a natural choice for optimal k -space coverage, as illustrated in Fig. 3. The spiral sampling window in k space [i.e., represented by a round tile, Fig. 3(a)] and the corresponding low-resolution sum image [$3.0 \times 3.0 \text{ mm}^2$, Fig. 3(b)] are shown as the references. With the diagonal tagging shortened to cover a rectangularly arranged pattern of the round tiles, certain regions between the neighboring tiles cannot be recovered in the reconstructed k -space data with resolution of $1.1 \times 1.1 \text{ mm}^2$ [see Fig. 3(c)], leading to visible image artifacts due to the k -space holes [see Fig. 3(d)]. These empty holes can be eliminated by uniformly reducing the neighboring bands' distance in all directions, but with a trade-off of a minimum of 29.3% band overlapping [see Fig. 3(e)], which compromises the resolution improvement potential leading to an image with resolution of $1.24 \times 1.24 \text{ mm}^2$ only [see Fig. 3(f)]. Therefore, the unscaled tagging in all directions is preferred for

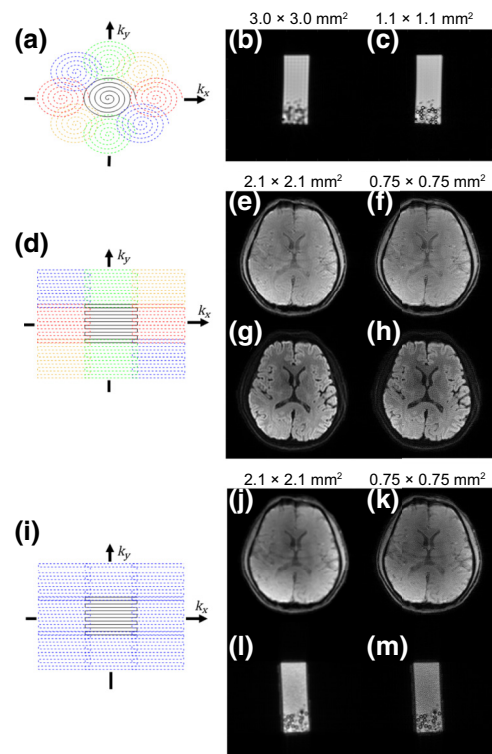


FIG. 2. Reconstruction of 2D threefold superresolution. (a) Reconstructed k -space bands, sampled by the spiral window at the center (black solid trajectory), with the side bands (red, blue, green, gold dotted trajectories), eventually resolve to reach a threefold enlarged circular coverage. (b) Sum of the low-resolution images with tagging, $3.0 \times 3.0 \text{ mm}^2$. (c) Reconstructed high-resolution image, $1.1 \times 1.1 \text{ mm}^2$. (d) Reconstructed k -space bands, sampled by the Cartesian window at the center (black solid trajectory), with the side bands (red, blue, green, gold dotted trajectories) eventually resolve to reach a rectangular threefold increased coverage. (e) Sum of the low-resolution nonweighted images with tagging, $2.1 \times 2.1 \text{ mm}^2$. (f) Reconstructed high-resolution nonweighted image, $0.75 \times 0.75 \text{ mm}^2$. (g) Sum of the low-resolution diffusion-weighted images (i.e., 16 diffusion directions) with tagging, $2.1 \times 2.1 \text{ mm}^2$. (h) Reconstructed high-resolution diffusion-weighted image (i.e., 16 diffusion directions), $0.75 \times 0.75 \text{ mm}^2$. No ghost artifact due to random phase fluctuation is observed, owing to the magnitude-based reconstruction. (i) Reconstructed k -space bands sampled by the Cartesian window at the center (black solid trajectory), with the side bands (blue dotted trajectory), resolve to form a rectangular threefold increased coverage. (j) Sum of low-resolution nonweighted images with tagging, $2.1 \times 2.1 \text{ mm}^2$. (k) Reconstructed high-resolution nonweighted image, $0.75 \times 0.75 \text{ mm}^2$. (l) Sum of low-resolution diffusion-weighted (i.e., 16 diffusion directions) images with tagging, $2.1 \times 2.1 \text{ mm}^2$. (m) Reconstructed high-resolution diffusion-weighted image (i.e., 16 diffusion directions), $0.75 \times 0.75 \text{ mm}^2$. The reconstruction is free of ghost artifacts in the presence of diffusion gradients due to the magnitude-based reconstruction. Please note that the k -space trajectories are drawn only for illustration purposes and are not strictly based on the scan protocols. Additionally, the details of reconstructed images can be visualized better in the full-size figure.

spiral acquisition, which maintains a continuous coverage of the enlarged final k -space window and has a very small requirement (7.6%) for the minimum band overlapping, yielding an image with resolution $1.1 \times 1.1 \text{ mm}^2$ [see Figs. 3(g) and 3(h)]. For both options with the spiral window, the minimum band overlapping is computed by the geometry of the k -space band patterns as illustrated in the Fig. 4.

B. Scheme B, 2D superresolution, 2D grid tagging

1. Tagging sequence

Scheme B concatenates two orthogonal tagging sequences with three shifts in each direction, modulating the object with a 2D grid pattern [see Fig. 1(f)], similar to multidoughnut nanoscopy [34]. This simultaneously covers nine k -space tiles [see Fig. 1(g)] arranged in a rectangular pattern similar to the rotational tagging with Cartesian sampling [Fig. 1(h)]. This grid tagging has been used for superresolution MRI [37] with a simplified, interleaving-based reconstruction, which does not provide the same resolution enhancement as the SIM-like reconstruction technique used here.

2. Reconstruction

Scheme B is tested by *in vivo* measurements with non-weighted images and diffusion-weighted phantom images. With a total of nine acquisitions by low-resolution Cartesian sampling [see Fig. 2(i), black solid trajectory], nine square k -space tiles are reconstructed and combined to reach approximately threefold increased k -space coverage in two orthogonal dimensions [see Fig. 2(i), side bands in blue dash trajectory]. From the low-resolution images [$2.1 \times 2.1 \text{ mm}^2$, their sum images are shown in Figs. 2(j) and 2(l)], high-resolution images with resolution of $0.75 \times 0.75 \text{ mm}^2$ (approximately 10% band overlapping) are reconstructed, with clearly more image details and no obvious artifacts [see Figs. 2(k) and 2(m)].

a. Comparisons between schemes A and B—Owing to the modulation of the net magnetization, scheme A has the relative SNR efficiency of 100% and 50% compared with the multishot segmented scan for regions covered by the tile at the k -space center and its neighbors, respectively. Scheme B maintains only 33% relative SNR efficiency for all bands because of the stronger suppression of the longitudinal magnetization by the grid tagging. While scheme A is preferred to maximize the SNR of phaseless encoding, scheme B requires three fewer acquisition cycles to complete the experiment. The SNR drop from scheme A to scheme B can be roughly observed by comparing the reconstruction [Fig. 2(f) versus Fig. 2(k); Fig. 2(h) versus Fig. 2(m)]. The calculation of the SNR performance is shown in the Supplemental Material [35].

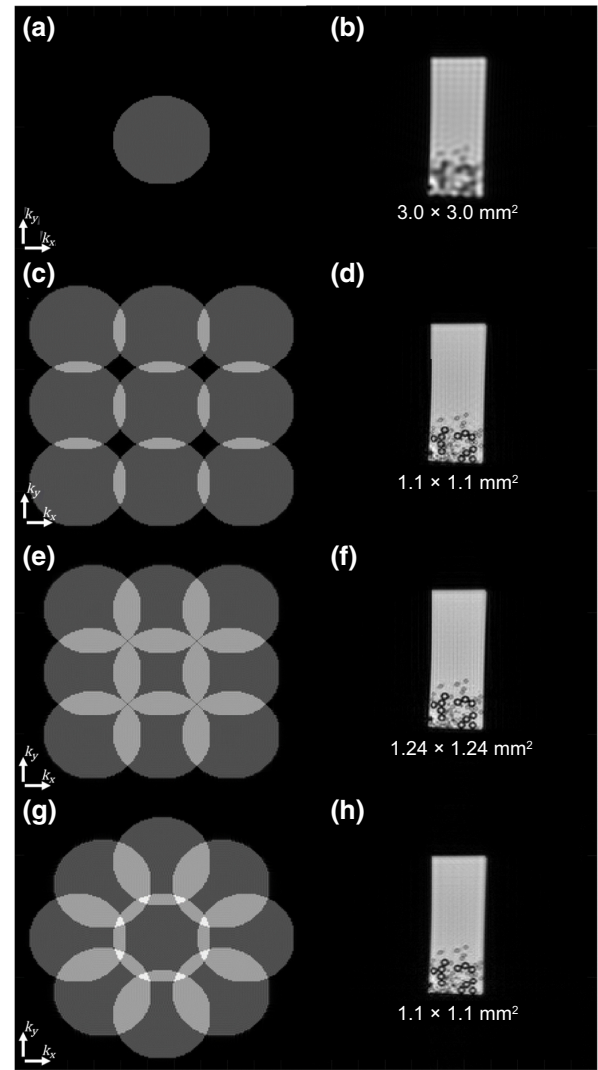


FIG. 3. Rectangularly and circularly arranged band pattern in k space for spiral acquisitions. (a) Low-resolution spiral sampling coverage. (b) Sum of low-resolution images with tagging, sampled by the spiral window in (a), $3.0 \times 3.0 \text{ mm}^2$. (c) High-resolution reconstructed k -space coverage using the rotated tagging scheme A. The tagging wavelength in the diagonal is shortened to yield a rectangularly arranged pattern, similar to the one in Cartesian 2D phaseless encoding, but incurs nonsampled k -space regions (i.e., holes) between neighboring bands. (d) Reconstructed image with the k -space coverage in (c), $1.1 \times 1.1 \text{ mm}^2$. (e) Reconstructed k -space coverage by uniformly increasing the tagging wavelength in the experiment in (c), eliminating the k -space holes between the reconstructed neighboring bands, but compromising the finally achieved resolution due to the large overlapped regions. (f) Reconstructed image with the k -space coverage in (e), $1.24 \times 1.24 \text{ mm}^2$. (g) Reconstructed k -space coverage by uniform tagging wavelength along all directions, resulting in a circularly arranged band pattern without large band overlapping. (h) Reconstructed images with the k -space coverage in (g), $1.1 \times 1.1 \text{ mm}^2$. Improved image quality can be seen in (h) compared with reconstructions in (d) and (f). The details of reconstructed images can be visualized better in the full-size figure.

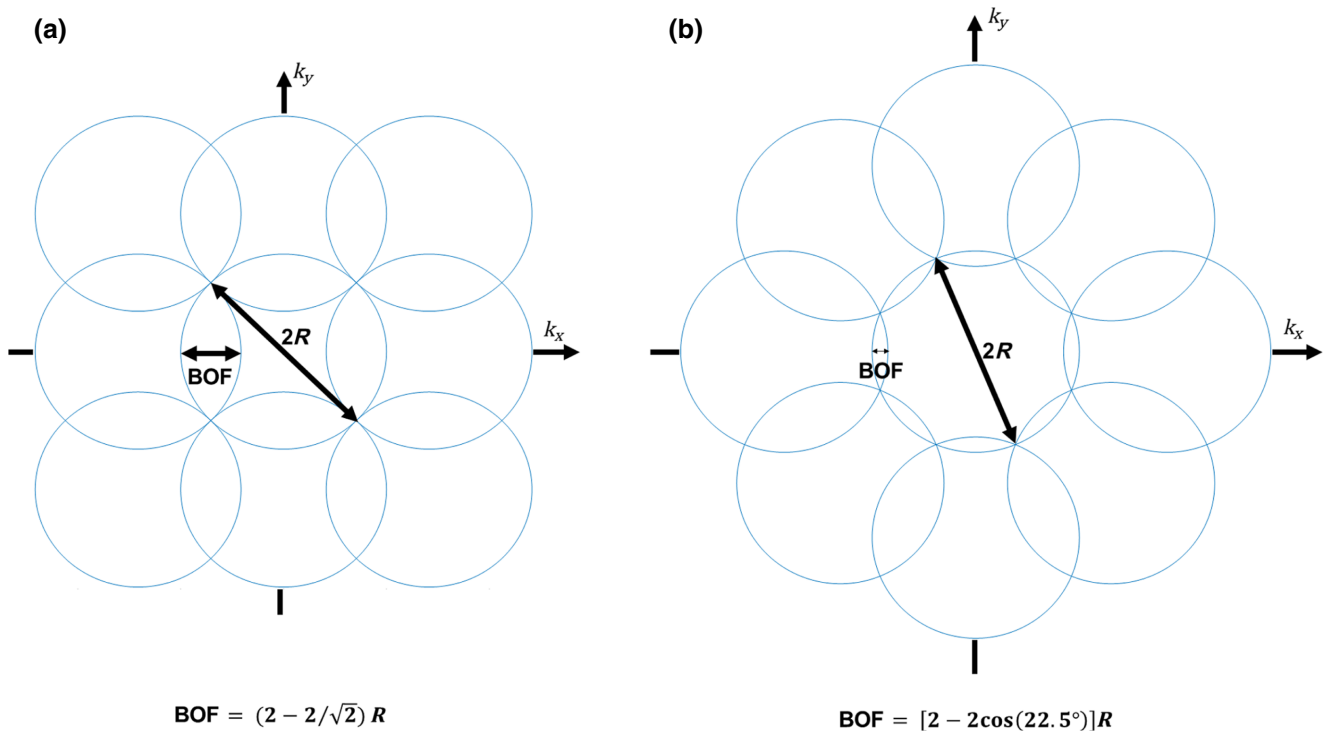


FIG. 4. The geometry of band overlapping for spiral acquisitions. R is the radius of each circular k -space band (i.e., coverage by spiral trajectory), BOF is the band overlapping factor, with the band overlapping percentage = $BOF/2R$. (a) Rectangular arrangement for 2D phaseless encoding with spiral, with the minimum band overlapping to avoid interband holes. In the finally reconstructed k -space data, along the k_x and the k_y directions, the maximum k -space range that can be reached is reduced by 29.3% of the single-shot circular coverage (i.e., by the low-resolution spiral trajectory), owing to strong band overlapping. (b) The circular arrangement with the minimum band overlapping to avoid holes, with only 7.6% band overlapping needed.

C. Scheme C, SSIM in MRI, 1D tagging with multiple wavelengths

1. Tagging sequence

Scheme C simultaneously samples the central band of the elongated EPI trajectory with two adjacent bands in the first three scans, similar to the standard 1D phaseless encoding, followed by a second set of three scans with the tagging shortened by half to cover the two bands twice this distance [see Fig. 1(i)]. In this way, multiple k -space signal bands are excited, reconstructed in separate scans [see Fig. 1(j), side bands in red, blue, yellow, and magenta], and eventually combined (with the central band averaged twice) to yield a fivefold superresolved image [equivalent to 5 times enlarged effective k -space coverage, see Fig. 1(k)].

Scheme C is tested with Cartesian sampling in the readout dimension for two different applications: to reach further resolution enhancement, and to reduce the echo spacing in each scan given the same final resolution. Compared with the multishot segmented scan, the relative SNR efficiency for scheme C is 75% and 53% for the central band and the side bands, respectively. The calculation of SNR performance for scheme C is shown in the Supplemental Material [35].

2. Reconstruction—higher resolution

The ability of the phaseless encoding to reach a super-resolution factor beyond 3 is demonstrated using a water phantom with small silicon tubes and with a human subject [see Figs. 5(a)–5(l)]. Sampled by a limited k -space window [see Fig. 5(d)], the sum of low-resolution images ($3.4 \times 0.75 \text{ mm}^2$) are shown as the reference for the water phantom, the nonweighted human head image, and the diffusion-weighted human head image with sum of 16 diffusion-weighted directions, respectively [see Figs. 5(a)–5(c)]. With standard 1D phaseless encoding, the reconstructed image resolution can be improved about threefold, as $1.25 \times 0.75 \text{ mm}^2$ [approximately 12% band overlapping, see Figs. 5(e)–5(h)]. Scheme C further enhances the spatial resolution around fivefold, reaching the resolution of $0.75 \times 0.75 \text{ mm}^2$ (approximately 12% band overlapping) and resolving more details than the threefold improved images [see Figs. 5(i)–5(l) in full size].

3. Reconstruction—reduced echo spacing

A human subject is scanned with scheme C to further shorten the EPI echo spacing while maintaining the same final resolution [see Figs. 5(m)–5(r) in full size]. The standard 1D threefold phaseless encoding improves

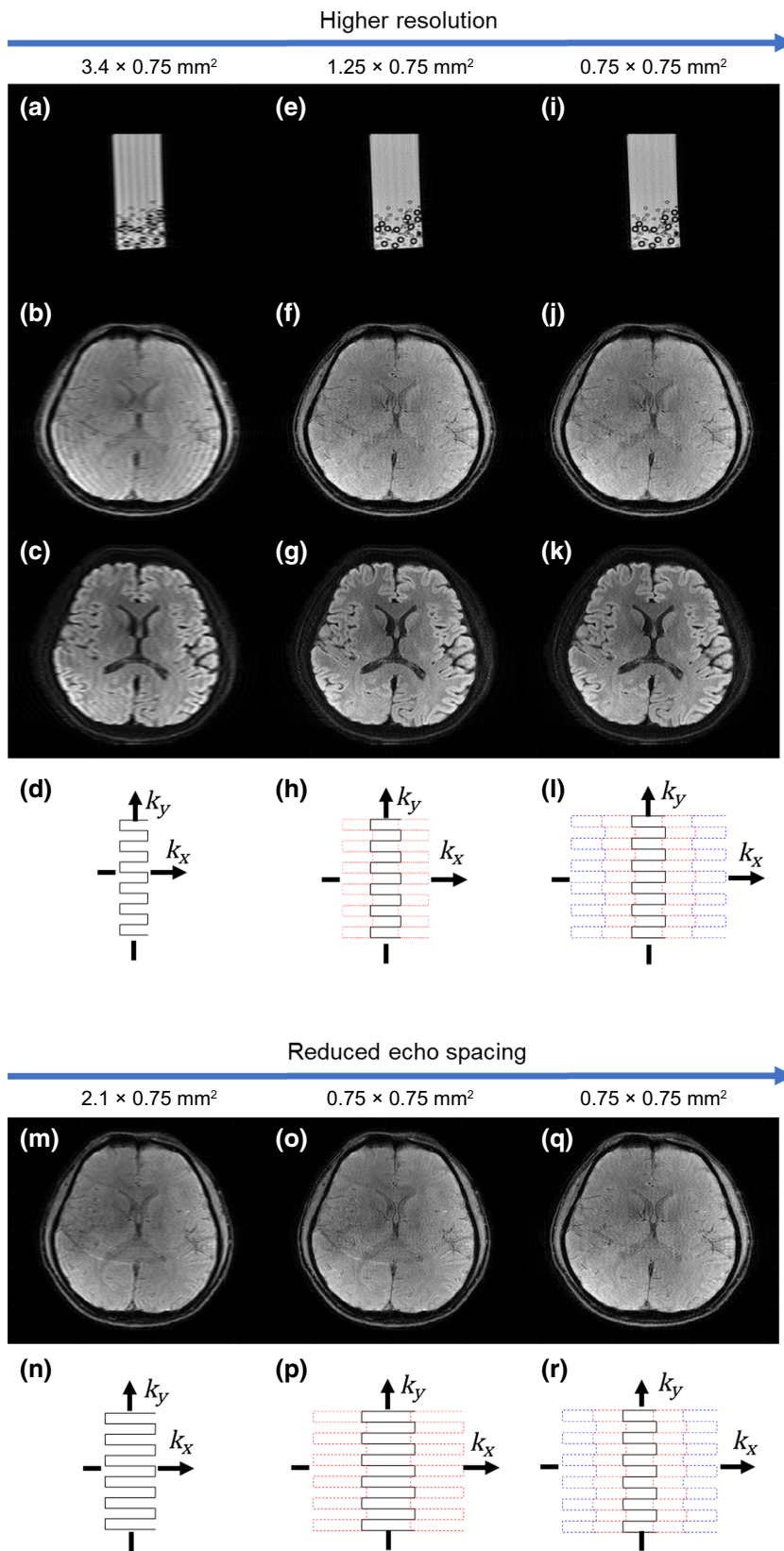


FIG. 5. The reconstruction of 1D fivefold superresolution for two applications. (a)–(c) Sum of low-resolution images with tagging for the water phantom with silicon tubes, the nonweighted head image, and the diffusion-weighted head image with 16 diffusion directions, respectively, all in $3.4 \times 0.75 \text{ mm}^2$. (d) The k -space coverage by the low-resolution EPI sampling. (e)–(g) Reconstructed image of the 1D threefold superresolution phaseless encoding, all in $1.25 \times 0.75 \text{ mm}^2$. (h) The k -space coverage by the standard 1D threefold phaseless encoding, with the low-resolution EPI sampling at the k -space center (black solid trajectory), and the two additional neighboring bands resolved in the reconstruction (red dotted trajectory). (i)–(k) Reconstructed image of the 1D fivefold superresolution phaseless encoding, all in $0.75 \times 0.75 \text{ mm}^2$. Note the diffusion images are free of ghost artifacts due to the magnitude-based reconstruction. (l) The k -space coverage by the 1D fivefold superresolution phaseless encoding with the low-resolution EPI sampling window (black solid trajectory), the two resolved bands for threefold higher spatial frequency (red dotted trajectory), and the two bands for fivefold higher spatial frequency resolved further. (m) Sum of low-resolution images with tagging for the nonweighted head image, in $2.1 \times 0.75 \text{ mm}^2$. (n) The k -space coverage by the low-resolution EPI sampling, which has longer echo time compared to the one in (d). (o) Reconstruction of the standard 1D threefold phaseless encoding for the nonweighted head image, in $0.75 \times 0.75 \text{ mm}^2$. (p) The k -space coverage by the standard 1D threefold phaseless encoding with the low-resolution EPI sampling at the k -space center (black solid trajectory), and the two additional neighboring bands resolved in the reconstruction (red dotted trajectory). (q) Reconstruction of the 1D fivefold phaseless encoding for the nonweighted head image, in the same final resolution as in (o), but with shorter echo spacing and, therefore, with visibly improved image quality. (r) The k -space coverage of the 1D fivefold phaseless encoding, reaching the same final resolution but with shorter echo spacing for the EPI window compared to (p). Please note that the k -space trajectories are drawn only for illustration purposes and are not strictly based on scan protocols. Additionally, the details of reconstructed images can be visualized better in the full-size figure.

the image resolution from $2.1 \times 0.75 \text{ mm}^2$ [see Fig. 5(m)] to $0.75 \times 0.75 \text{ mm}^2$ (approximately 10% band overlapping) [see Fig. 5(o)]. By applying scheme C, the same

final resolution can be achieved with even shorter echo spacing, in which a superresolution image with resolution $0.75 \times 0.75 \text{ mm}^2$ [see Fig. 5(q)] can be reconstructed

from low-resolution tagged images [$3.4 \times 0.75 \text{ mm}^2$, see Fig. 5(b)]. The corresponding k -space coverage for each image can be visualized in Figs. 5(n), 5(p), and 5(r), as well as Fig. 5(d). The possibility to acquire images with shorter echo spacing can lead to better image quality, such as having less geometric distortion in the presence of field inhomogeneity.

III. TECHNICAL DETAILS FOR IMPLEMENTATION

All experiments are carried out on a 3-Tesla MRI scanner equipped with 30 mT/m, 200 T/m/s gradients (Achieva 3-Tesla, Philips Healthcare, Netherlands) and an eight-channel head array receiver coil using our own modification of the manufacturer's sequence code. Acquired data are reconstructed offline using non-Cartesian rf sensitivity encoding (SENSE) and k -space gridding based on a trajectory measured concurrently with a field camera (Skopec, Switzerland). A rectangular water-filled phantom with immersed silicon tubes (1.5-mm wall thickness) and a spherical phantom are used for phantom scans, and a healthy male adult volunteered for the *in vivo* scans in agreement with the institution's ethics policy.

A. The general MRI scan protocols

The field of view (FOV) for all scans is $220 \times 220 \text{ mm}^2$, except for the scan of the spherical phantom with $280 \times 280 \text{ mm}^2$. The repetition time interval is 3s for EPI (Cartesian) and spiral scans. The echo time is 12–13 ms for EPI (Cartesian) acquisition, and 2.2 ms for spiral acquisition. The slice thickness is around 2 to 3 mm, and the time duration between rf binomial pulses in the tagging sequence is around 2 to 3 ms. The tagging flip angle is set to be around 45° or 54.7° . The isotropic diffusion-weighted image is calculated by averaging images obtained with 16 directions of diffusion-sensitizing gradients, with b value 800 s/mm^2 .

B. The specific protocols for schemes A–C

1. Scheme A, 1D rotational tagging

a. Circular arrangement—Figs. 2(a)–2(c), 3(g) and 3(h)—Each phaseless encoding experiment along a rotated direction acquires three low-resolution images with resolution of 3 mm (readout, horizontal) \times 3 mm (phase, vertical) by a single shot of spiral sampling (acquisition window of 35 ms). During each acquisition, the tagging pattern with period of 3.5 mm (which corresponds to 14.2% band overlapping) is phase shifted by 0° , 120° , and 240° , respectively. This experiment is repeated in the four directions (horizontal, vertical, diagonals) with the identical tagging period. A high-resolution image with resolution of

1.1 mm (readout, horizontal) \times 1.1 mm (phase, vertical) is reconstructed.

b. Rectangular arrangement—Figs. 2(d)–2(h)—Each phaseless encoding experiment acquires three low-resolution images with resolution of 2.1 mm (readout, horizontal) \times 2.1 mm (phase, vertical) by EPI sampling. It is repeated in four directions (horizontal, vertical, diagonals), with the tagging periods of 2.34 mm in horizontal and vertical scans, and 1.65 mm in diagonal scans, corresponding to about 10% band overlapping. The tagging pattern is shifted by 0° , 120° , and 240° in each experiment along a direction. A high-resolution image with resolution of 0.75 mm (readout, horizontal) \times 0.75 mm (phase, vertical) is reconstructed.

c. Rectangular arrangement—Figs. 3(c)–3(f)—Each phaseless encoding scan acquires three low-resolution images with resolution of 3.0 mm (readout, horizontal) \times 3.0 mm (phase, vertical) by a single shot of spiral sampling (acquisition window of 35 ms), and with tagging pattern (along readout and phase directions) in the period of 3.5 mm [see Fig. 3(c)] and 4.25 mm [see Fig. 3(e)], corresponding to 14.2% and 29.4% band overlapping, respectively. The tagging pattern is shifted by 0° , 120° , and 240° in each experiment along a direction. The reconstructed high-resolution images are $1.1 \times 1.1 \text{ mm}^2$ [see Fig. 3(d)] and $1.24 \times 1.24 \text{ mm}^2$ [see Fig. 3(f)], respectively.

2. Scheme B, 2D grid tagging, rectangular arrangement

In Figs. 2(j) and 2(l) and the low-resolution scans for the reconstruction in Figs. S3(e) and S3(f) in the Supplemental Material [35], the phaseless encoding scan acquires nine low-resolution images with resolution of 2.1 mm (readout, horizontal) \times 2.1 mm (phase, vertical) by EPI sampling. The 2D tagging can be seen as the multiplication of two orthogonal 1D tagging (i.e., [horizontal; vertical]), each with period of 2.34 mm, but with independent phase shifts during each scan [tag x ; tag y] as: $[0^\circ; 0^\circ]$, $[0^\circ; 120^\circ]$, $[0^\circ; 240^\circ]$, $[120^\circ; 0^\circ]$, $[120^\circ; 120^\circ]$, $[120^\circ; 240^\circ]$, $[240^\circ; 0^\circ]$, $[240^\circ; 120^\circ]$, $[240^\circ; 240^\circ]$.

A similar protocol is used for the low-resolution scans, from which the spherical phantom in Figs. S3(c) and S3(d) in the Supplemental Material [35] are reconstructed. However, in these scans, the FOV is $280 \times 280 \text{ mm}^2$, and the tagging period is 3.2 mm (readout, horizontal) \times 3.2 mm (phase, vertical).

The high-resolution with resolution of 0.75 mm (readout, horizontal) \times 0.75 mm (phase, vertical) is reconstructed corresponding to 10% band overlapping, as in Figs. 2(k) and 2(m), and Figs. S3(c)–S3(f) in the Supplemental Material [35]. Note that the reconstructions in Figs. S3(c) and S3(e) in the Supplemental Material [35] are

not corrected with the estimated residue B_0 related phase errors.

3. Scheme C, 1D tagging with multiple wavelengths, five-band arrangement in 1D

In Figs. 5(a)–5(c), the phaseless encoding experiment acquires three low-resolution images with resolution of 3.4 mm (readout, horizontal) \times 0.75 mm (phase, vertical) by EPI sampling. This is repeated twice with tagging periods of 3.85 and 1.925 mm, respectively, and each one has the tagging shifts of 0° , 120° , and 240° .

In Figs. 5(e)–5(g) and 5(i)–5(k), high-resolution images in 1.25 mm (readout, horizontal) \times 0.75 mm (phase, vertical) and 0.75 mm (readout, horizontal) \times 0.75 mm (phase, vertical) are reconstructed, respectively achieving almost threefold and fivefold superresolution in the readout dimension with around 12% band overlapping.

In Fig. 5(m), the phaseless encoding scan acquires low-resolution images with resolution of 2.1 mm (readout, horizontal) \times 0.75 mm (phase, vertical) by EPI sampling, and tagging period of 2.35 mm in shifts of 0° , 120° , and 240° .

In Fig. 5(o), a high-resolution image with 0.75 mm (readout, horizontal) \times 0.75 mm (phase, vertical) is reconstructed with band overlapping of about 10%, reaching almost threefold resolution enhancement.

Figure 5(q) is identical to Fig. 5(j), and therefore, has the same protocol.

C. Phaseless encoding image reconstruction

The raw data after SENSE and partial Fourier reconstruction are loaded into the phaseless encoding reconstruction pipeline to obtain the final high-resolution image, similar to the previous work [28]. In the experiments here, schemes *A* and *C* have the central band averaged multiple times, and scheme *B* has nine bands (nine unknowns) to resolve instead of three. The inverse filter calculated from the propagated low-resolution apodized window are shown in Fig. S2 in Supplemental Material [35].

(1) Low resolution images from each scan are reconstructed using non-Cartesian SENSE and Fourier transformed back to k space.

(2) The obtained low-resolution k -space data, which still contain mixed signal bands, are apodized by a Kaiser filter with the width factor from 2.7 to 3.

(3) The apodized data are inverse Fourier transformed to the image space and the magnitude is taken to eliminate the shot-dependent phase fluctuations.

(4) The magnitude images are Fourier transformed to the k space and the mixed bands' signals are resolved by inversion of the linear problem represented by one of the Eqs. (S6)–(S8) in the Supplemental Material [35].

(5) For the tagging schemes *A* and *C*, the resolved bands in each scan are combined to reconstruct k -space data with increased coverage. The tagging scheme *B* directly obtains all bands after resolving nine shots of acquired images.

(6) The reconstructed k -space bands are multiplied by the inverse filters calculated from the apodization window in the first step. The inverse filters efficiently eliminate the amplitude modulation by different band overlaps as shown in Fig. S2 in Supplemental Material [35].

(7) Optionally, the reconstructed k -space bands are corrected by the additionally acquired B_0 and B_1 maps for tagging distortions. A small array of pixels around the side band centers are zero-filled to reduce amplitude fluctuations between shots. In scheme *B*, residue phase offsets after the B_0 map tagging correction are estimated by comparing overlapped regions between neighboring bands and used for phase offset corrections (see Fig. S3 in Supplemental Material [35]).

(8) Finally, the reconstructed k -space data with larger coverage are transformed to the image domain to obtain the superresolution image.

IV. CONCLUSION AND DISCUSSION

Phaseless encoding is successfully used to reach a threefold resolution enhancement in two dimensions and a fivefold enhancement in one dimension, which demonstrates the utility of SIM and SSIM superresolution concepts in MRI. This approach enables multishot high-resolution MRI scanning based on the absolute value of intermediate low-resolution images, freeing it from the usual intershot phase sensitivity, in particular in the context of diffusion-weighted imaging. With the extensions presented in this work, this superresolution technique becomes compatible with arbitrary k -space sampling trajectories in MRI, and has no inherent limit on the maximum resolution enhancement factor. Based on these concepts, experiments for improving resolution in three orthogonal dimensions or beyond the fivefold superresolution will be straightforward to implement by modifying the tagging schemes *A*–*C* to excite and resolve more k -space signal bands in a similar manner. The applications of this technique in fMRI and direct comparisons with alternative phase-insensitive MRI methods [38–40] represent a highly interesting topic for future studies.

However, a fundamental limit for such resolution enhancements—the SNR of the reconstructed image—will eventually be reached when the signal energy contributing to a single pixel becomes too low relative to the constant noise power. Therefore, the ultimate resolution for phaseless encoding MRI depends on the minimum SNR requirement and the maximum scan time for averaging, without considering the limit imposed by the diffusion phenomenon. This also applies for the conventional multishot segmented scans.

Implementing structured illumination in MRI does not require additional hardware and demands only a minor modification to the preparatory part of existing MRI pulse sequences. Given the characteristics of the tagging sequence, the illumination pattern in MRI can reach slightly negative values to excite k -space signal bands with equal amplitude to maximize the SNR. At the same time, the wavelength of the MRI pattern can be arbitrarily smaller than the pixel size and provide an arbitrary resolution enhancement (limited only by SNR), in contrast to SIM where the illumination itself is diffraction limited and the resolution can only be tripled. In addition, nonlinear illumination patterns can also be generated using properties of the steady-state magnetization without the need for additional preparatory sequences, as demonstrated recently [41]. Presented analogies between optical SR methods and MRI surely do not exhaust all possibilities to transfer ideas between these two seemingly distant, but, in fact, closely related imaging modalities. Thus, we believe this path is worth exploring further.

ACKNOWLEDGMENTS

R.T. contributed to the concepts of presented methods, implemented the MRI sequences and reconstruction

algorithms, and carried out the experimental work. F.H. developed the basic concepts, contributed to the implementation, and edited the paper together with R.T. S.B. developed the method of resolution assessment. K.P.P. supervised the conceptual, experimental, and editing work.

APPENDIX: EVALUATION OF EFFECTIVE RESOLUTION ENHANCEMENT

Throughout the paper the resolution of the SR images is provided as the inverse of the k -space range recovered from the phaseless encoding reconstruction. This definition is verified by an analysis of image contours of a spherical phantom. Radial sections through the contours allow the measurement of edge-spread functions in multiple directions. Their derivatives correspond to projections of the 2D point-spread function (PSF) in these directions. By virtue of the central slice theorem, the Fourier transforms of these projections represent sections of the 2D modulation transfer function (MTF), the 2D Fourier transform of the PSF. A map of the MTF, which can be obtained from the sections by interpolation, shows the k -space region that effectively contributes to the image. This procedure is a generalization of the 1D resolution assessment method based on linear contours proposed by Delakis *et al.* [36] (Fig. 6).

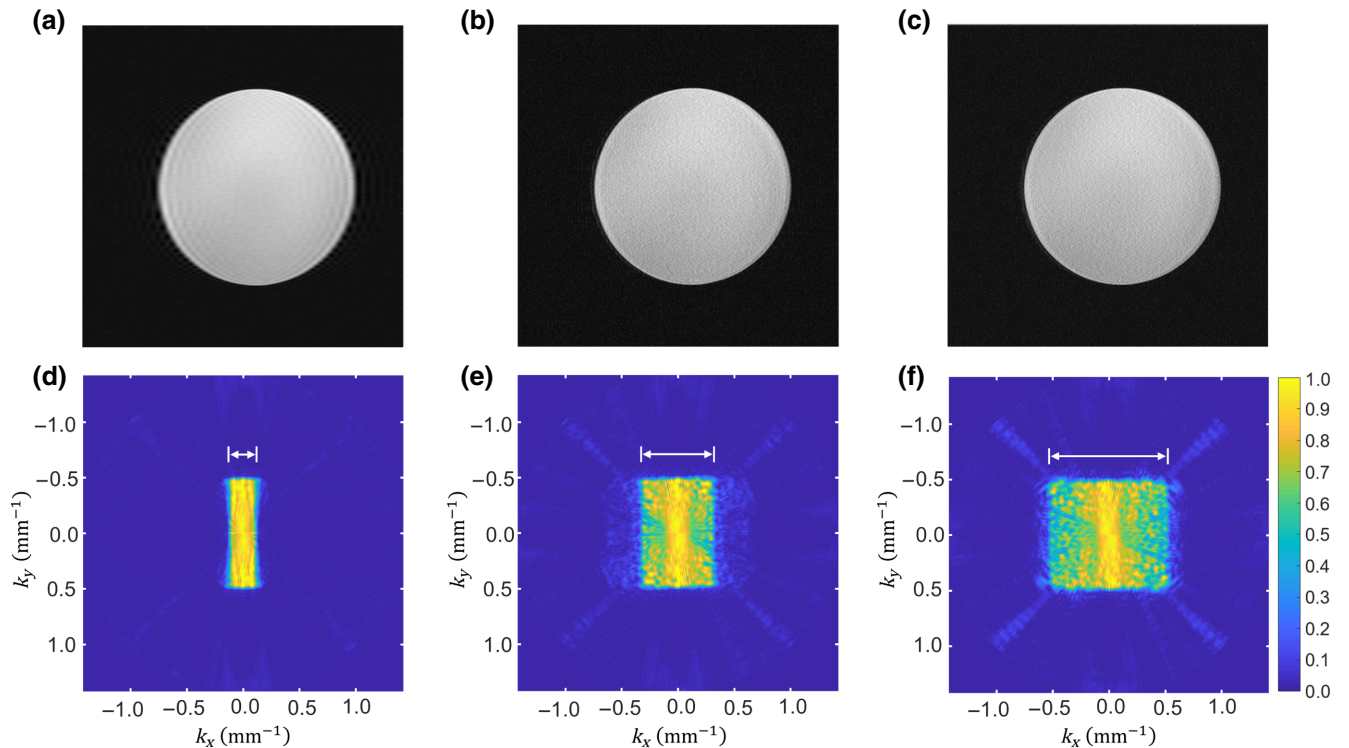


FIG. 6. The MTF analysis for a low-resolution image and two superresolution images with threefold and fivefold resolution improvement by phaseless encoding. (a) Low-resolution image, nominal resolution of 4.0 mm (horizontal) \times 1.0 mm (vertical). (b) Threefold resolution enhanced image, nominal resolution of 1.53 mm (horizontal) \times 1.0 mm (vertical). (c) Fivefold resolution enhanced image, nominal resolution of 0.95 mm (horizontal) \times 1.0 mm (vertical). (d) The MTF map calculated from (a). (e) The MTF map calculated from (b). (f) The MTF map calculated from (c). (d)–(f) are shown as linear color maps with arbitrary units.

Figure 6 shows the MTF analysis for a low-resolution image (resolution 4.0 mm horizontally, 1.0 mm vertically, upper row, *a*), and two superresolution images (nominal horizontal resolution 1.53 and 0.95 mm, respectively; vertical resolution unchanged) obtained with 1D tagging to achieve nearly threefold (*b*) and fivefold (*c*) resolution enhancement, as described in scheme C. The bottom row shows the MTF maps calculated from these images (linear color map with arbitrary units). The width of the MTF support closely matches the theoretical k -space range (arrows), which confirms the correctness of the resolution measure adopted in this work.

-
- [1] P. C. Lauterbur, Image formation by induced local interactions: Examples employing nuclear magnetic resonance, *Nature* **242**, 190 (1973).
- [2] P. Mansfield and P. K. Grannell, NMR ‘diffraction’ in solids?, *J. Phys. C: Solid State Phys.* **6**, L422 (1973).
- [3] P. Mansfield and P. K. Grannell, ‘Diffraction’ and microscopy in solids and liquids by NMR, *Phys. Rev. B* **12**, 3618 (1975).
- [4] S. Ljunggren, A simple graphical representation of Fourier-based imaging methods, *J. Magn. Reson.* **54**, 338 (1983).
- [5] D. B. Twieg, The k -trajectory formulation of the NMR imaging process with applications in analysis and synthesis of imaging methods, *Med. Phys.* **10**, 610 (1983).
- [6] R. S. Likes, Moving gradient zeugmatography. US Patent #4307343 issued (22 Dec 1981).
- [7] P.-F. Van de Moortele, J. Pfeuffer, G. H. Glover, K. Ugurbil, and X. Hu, Respiration-induced B0 fluctuations and their spatial distribution in the human brain at 7 Tesla, *Magn. Reson. Med.* **47**, 888 (2002).
- [8] P. J. Basser, J. Mattiello, and D. LeBihan, MR diffusion tensor spectroscopy and imaging, *Biophys. J.* **66**, 259 (1994).
- [9] S. Ogawa, D. W. Tank, R. Menon, J. M. Ellermann, S. G. Kim, H. Merkle, and K. Ugurbil, Intrinsic signal changes accompanying sensory stimulation: Functional brain mapping with magnetic resonance imaging, *Proc. Natl. Acad. Sci. U. S. A.* **89**, 5951 (1992).
- [10] K. K. Kwong, J. W. Belliveau, D. A. Chesler, I. E. Goldberg, R. M. Weisskoff, B. P. Poncelet, D. N. Kennedy, B. E. Hoppel, M. S. Cohen, and R. Turner, Dynamic magnetic resonance imaging of human brain activity during primary sensory stimulation, *Proc. Natl. Acad. Sci. U. S. A.* **89**, 5675 (1992).
- [11] P. A. Bandettini, E. C. Wong, R. S. Hinks, R. S. Tikofsky, and J. S. Hyde, Time course EPI of human brain function during task activation, *Magn. Reson. Med.* **25**, 390 (1992).
- [12] P. Mansfield, Multi-planar image formation using NMR spin echoes, *J. Phys. C: Solid State Phys.* **10**, L55 (1977).
- [13] C. B. Ahn, J. H. Kim, and Z. H. Cho, High-speed spiral-scan echo planar NMR imaging-I, *IEEE Trans. Med. Imaging* **5**, 2 (1986).
- [14] S. Bretschneider, C. Eggeling, and S. W. Hell, Breaking the Diffraction Barrier in Fluorescence Microscopy by Optical Shelving, *Phys. Rev. Lett.* **98**, 218103 (2007).
- [15] S. W. Hell and M. Kroug, Ground-state-depletion fluorescence microscopy: A concept for breaking the diffraction resolution limit, *Appl. Phys. B: Lasers Opt.* **60**, 495 (1995).
- [16] S. Bretschneider, C. Eggeling, and S. W. Hell, Breaking the Diffraction Barrier in Fluorescence Microscopy by Optical Shelving, *Phys. Rev. Lett.* **98**, 218103 (2007).
- [17] E. Betzig, G. H. Patterson, R. Sougrat, O. W. Lindwasser, S. Olenych, J. S. Bonifacino, M. W. Davidson, J. Lippincott-Schwartz, and H. F. Hess, Imaging intracellular fluorescent proteins at nanometer resolution, *Science* **313**, 1642 (2006).
- [18] M. J. Rust, M. Bates, and X. Zhuang, Sub-diffraction-limit imaging by stochastic optical reconstruction microscopy (STORM), *Nat. Methods* **3**, 793 (2006).
- [19] R. Heintzmann and C. G. Cremer, in *Proc. SPIE 3568, Optical Biopsies and Microscopic Techniques III* vol. 3568 (1999), pp. 185–197.
- [20] M. G. L. Gustafsson, Surpassing the lateral resolution limit by a factor of two using structured illumination microscopy, *J. Microsc.* **198**, 82 (2000).
- [21] J. T. Frohn, H. F. Knapp, and A. Stemmer, True optical resolution beyond the Rayleigh limit achieved by standing wave illumination, *Proc. Natl. Acad. Sci. U. S. A.* **97**, 7232 (2000).
- [22] R. Heintzmann, T. M. Jovin, and C. Cremer, Saturated patterned excitation microscopy—a concept for optical resolution improvement, *J. Opt. Soc. Am. A* **19**, 1599 (2002).
- [23] R. Heintzmann, Saturated patterned excitation microscopy with two-dimensional excitation patterns, *Micron* **34**, 283 (2003).
- [24] M. G. L. Gustafsson, Nonlinear structured-illumination microscopy: Wide-field fluorescence imaging with theoretically unlimited resolution, *Proc. Natl. Acad. Sci. U. S. A.* **102**, 13081 (2005).
- [25] L. Axel and L. Dougherty, MR imaging of motion with spatial modulation of magnetization, *Radiology* **171**, 841 (1989).
- [26] F. Hennel and K. P. Pruessmann, MRI with phaseless encoding, *Magn. Reson. Med.* **78**, 1029 (2017).
- [27] F. Hennel, R. Tian, M. Engel, and K. P. Pruessmann, In-plane “superresolution” MRI with phaseless sub-pixel encoding, *Magn. Reson. Med.* **80**, 2384 (2018).
- [28] R. Tian, F. Hennel, and K. P. Pruessmann, Low-distortion diffusion tensor MRI with improved phaseless encoding, *J. Magn. Reson.* **309**, 106602 (2019).
- [29] G. V. Steenkiste, B. Jeurissen, J. Veraart, A. J. D. Dekker, P. M. Parizel, D. H. J. Poot, and J. Sijbers, Super-resolution reconstruction of diffusion parameters from diffusion-weighted images with different slice orientations, *Magn. Reson. Med.* **75**, 181 (2016).
- [30] K. Setsompop, Q. Fan, J. Stockmann, B. Bilgic, S. Huang, S. F. Cauley, A. Nummenmaa, F. Wang, Y. Rathi, T. Witzel, and L. L. Wald, High-resolution in vivo diffusion imaging of the human brain with generalized slice dithered enhanced resolution: Simultaneous multislice (gSlider-SMS), *Magn. Reson. Med.* **79**, 141 (2018).
- [31] R. Tian, F. Hennel, and K. P. Pruessmann, in *Program #2671. In proceedings of the joint annual meeting of ISMRM-ESMRMB 2018, Paris, France* (June, 2018).

- [32] R. Tian, F. Hennel, and K. P. Pruessmann, in *Program #4675. In proceedings of the joint annual meeting of ISMRM 2019*, Montreal, Canada (May, 2019).
- [33] E. M. Haacke, Y. Xu, Y.-C. N. Cheng, and J. R. Reichenbach, Susceptibility weighted imaging (SWI), *Magn. Reson. Med.* **52**, 612 (2004).
- [34] A. Chmyrov, J. Keller, T. Grotjohann, M. Ratz, E. d'Este, S. Jakobs, C. Eggeling, and S. W. Hell, Nanoscopy with more than 100,000 'doughnuts', *Nat. Methods* **10**, 737 (2013).
- [35] See Supplemental Material at <http://link.aps.org/supplemental/10.1103/PhysRevApplied.19.034074> for more mathematical formulation and technical backgrounds of the phaseless encoding method presented in this paper.
- [36] I. Delakis, C. Xanthis, and R. I. Kitney, Assessment of the limiting spatial resolution of an MRI scanner by direct analysis of the edge spread function, *Med. Phys.* **36**, 1637 (2009).
- [37] S. Ropele, F. Ebner, F. Fazekas, and G. Reishofer, Super-resolution MRI using microscopic spatial modulation of magnetization, *Magn. Reson. Med.* **64**, 1671 (2010).
- [38] D. A. Porter and R. M. Heidemann, High resolution diffusion-weighted imaging using readout-segmented echo-planar imaging, parallel imaging and a two-dimensional navigator-based reacquisition: EPI with parallel imaging and 2D reacquisition, *Magn. Reson. Med.* **62**, 468 (2009).
- [39] N.-K. Chen, A. Guidon, H.-C. Chang, and A. W. Song, A robust multi-shot scan strategy for high-resolution diffusion weighted MRI enabled by multiplexed sensitivity-encoding (MUSE), *NeuroImage* **72**, 41 (2013).
- [40] M. Mani, M. Jacob, D. Kelley, and V. Magnotta, Multi-shot sensitivity-encoded diffusion data recovery using structured low-rank matrix completion (MUSSELS), *Magn. Reson. Med.* **78**, 494 (2017).
- [41] P. J. Lally, P. M. Matthews, and N. K. Bangerter, Unbalanced SSFP for super-resolution in MRI, *Magn. Reson. Med.* **85**, 2477 (2021).

Correction: The label on the previously published Figures 2(b) and 3(b) was erroneously changed during the production cycle and has been set right.